

Brian Gawlik¹

Department of Mechanical Engineering,
NASCENT Center,
The University of Texas at Austin,
Austin, TX 78758
e-mail: brian.gawlik@utexas.edu

Ariel R. Barr

Department of Physics,
NASCENT Center,
The University of Texas at Austin,
Austin, TX 78758
e-mail: beso_de_angel@utexas.edu

Akhila Mallavarapu

Department of Mechanical Engineering,
NASCENT Center,
The University of Texas at Austin,
Austin, TX 78758
e-mail: akhila@utexas.edu

Edward T. Yu

Department of Electrical and
Computer Engineering,
The University of Texas at Austin,
NASCENT Center,
Austin, TX 78758
e-mail: ety@ece.utexas.edu

S. V. Sreenivasan

Department of Mechanical Engineering,
NASCENT Center,
The University of Texas at Austin,
Austin, TX 78758
e-mail: sv.sreeni@mail.utexas.edu

Spectral Imaging and Computer Vision for High-Throughput Defect Detection and Root-Cause Analysis of Silicon Nanopillar Arrays

Far-field spectral imaging, coupled with computer vision methods, is demonstrated as an effective inspection method for detection, classification, and root-cause analysis of manufacturing defects in large area Si nanopillar arrays. Si nanopillar arrays exhibit a variety of nanophotonic effects, causing them to produce colors and spectral signatures which are highly sensitive to defects, on both the macro- and nanoscales, which can be detected in far-field imaging. Compared with traditional nanometrology approaches like scanning electron microscopy (SEM), atomic force microscopy (AFM), and optical scatterometry, spectral imaging offers much higher throughput due to its large field of view (FOV), micrometer-scale imaging resolution, sensitivity to nm-scale feature geometric variations, and ability to be performed in-line and nondestructively. Thus, spectral imaging is an excellent choice for high-speed defect detection/classification in Si nanopillar arrays and potentially other types of large-area nanostructure arrays (LNAs) fabricated on Si wafers, glass sheets, and roll-to-roll webs. The origins of different types of nano-imprint patterning defects—including particle voids, etch delay, and nonfilling—and the unique ways in which they manifest as optical changes in the completed nanostructure arrays are discussed. With this understanding in mind, computer vision methods are applied to spectral image data to detect and classify various defects in a sample containing wine glass-shaped Si resonator arrays. [DOI: 10.1115/1.4049959]

Introduction

Modern high-throughput nanopatterning techniques such as nano-imprint lithography [1] make it possible to fabricate arrays of nanostructures (features with dimensions of tens to hundreds of nm) over large area substrates (cm² to m² scale) such as Si wafers, glass sheets, and flexible roll-to-roll (R2R) webs. So-called “large-area nanostructure arrays” (LNAs) include, but are not limited to, gratings, mesh patterns, and pillar arrays, which each can serve as building blocks for a variety of unique applications. Metal nanograting patterns, for instance, can be used as wire-grid polarizers (WGP) [2], which promise efficiency increases in liquid crystal displays (LCDs). Metal mesh grids (MMGs) can be utilized as a cheap, flexible alternative to metal oxide layers (e.g., indium tin oxide) for transparent conducting films [3–5]. Arrays of Si nanopillars are also being looked to for an extensive list of applications including gas sensing [6–8], optical sensing [9–11], battery technology [12], ultracapacitors [13,14], and memory devices [15–17], as well as for color filtering in printing [18,19], displays, and imaging devices [11].

The leap from the research environment to high volume manufacturing will require deployment of advanced metrology systems as well as fabrication systems. Metrology is needed to provide detection, classification, and root-cause analysis of defects as they

appear in the manufacturing process, particularly during the scale-up phase. Unfortunately, whereas fabrication systems are ready for LNAs, existing nanometrology solutions are not viable because they are not well suited for scaling to very high manufacturing throughput. Techniques like scanning electron microscopy (SEM) and atomic force microscopy (AFM), which have been used extensively in the semiconductor industry, focus on measuring feature geometry directly, which is inherently slow because to do so with high accuracy constrains the field of view (FOV) of these measurements to the micron-scale. Considering that LNA device areas may be m² scale, exhaustive characterization would be prohibitively time consuming, even with multibeam techniques, such as Zeiss’s multibeam SEM, which is self-reported to take 3 h for a 1 cm² area [20]. Furthermore, three-dimensional SEM measurements often require sample destruction—such as in the case of cross-sectional SEM—which makes them ineffective for quality inspection of outgoing products. Traditional forms of optical scatterometry, another geometric metrology method, will also have extreme difficulty keeping pace, because despite having larger FOV than microscopy methods (hundreds of micrometer to mm scale), they still measure samples one point at a time, severely limiting throughput.

In actuality, the geometry of nanofeatures does not necessarily need to be determined to detect defects or even to determine their root cause. In LNAs, many types of defects, including those resulting from nanoscale geometric variations, can be identified visually on the macroscale due to optical changes induced by the defects. This is because, by virtue of their scale, LNAs exhibit nanophotonic effects, creating a range of optical signatures that

¹Corresponding author.

Contributed by the Manufacturing Engineering Division of ASME for publication in the JOURNAL OF MICRO- AND NANO-MANUFACTURING. Manuscript received March 1, 2020; final manuscript received September 14, 2020; published online February 26, 2021. Assoc. Editor: Michael Cullinan.

can be observed visually. Si nanopillar arrays, for instance, exhibit structural coloration as a result of a variety of nanophotonic phenomena including Mie resonance [18,19,21], Fabry-Perot resonance, and guided modes [22]. Figure 1 shows the relationship between geometry, color, and reflectance spectra for a handful of different Si nanopillar arrays which we have fabricated including hourglass-shaped and wine glass-shaped resonators, truncated cones, and high aspect ratio nanowire arrays created using metal-assisted chemical etching (MACE) [14]. Each of these structures creates unique colorful properties, which are extremely sensitive to small variations in feature geometry (e.g., diameter or height). The hourglass-shaped Si nanopillars shown in Fig. 1(a), for

instance, exhibit size-dependent Mie resonance and change from blue to green when their average diameter increases by just ~ 10 to 20 nm. Even more dramatic are the visual changes the arrays undergo in the presence of macroscale patterning defects like particle contamination and etch errors.

Because of these colorful optical signatures, defect detection can be done over large areas with micrometer-scale imaging resolution and sensitivity to nm-scale variations in feature geometry, using spectral imaging systems such as RGB or hyperspectral cameras. Spectral imaging systems are available and used in the semiconductor industry today for defect inspection, although to our knowledge, the specific link between nanophotonic structures,

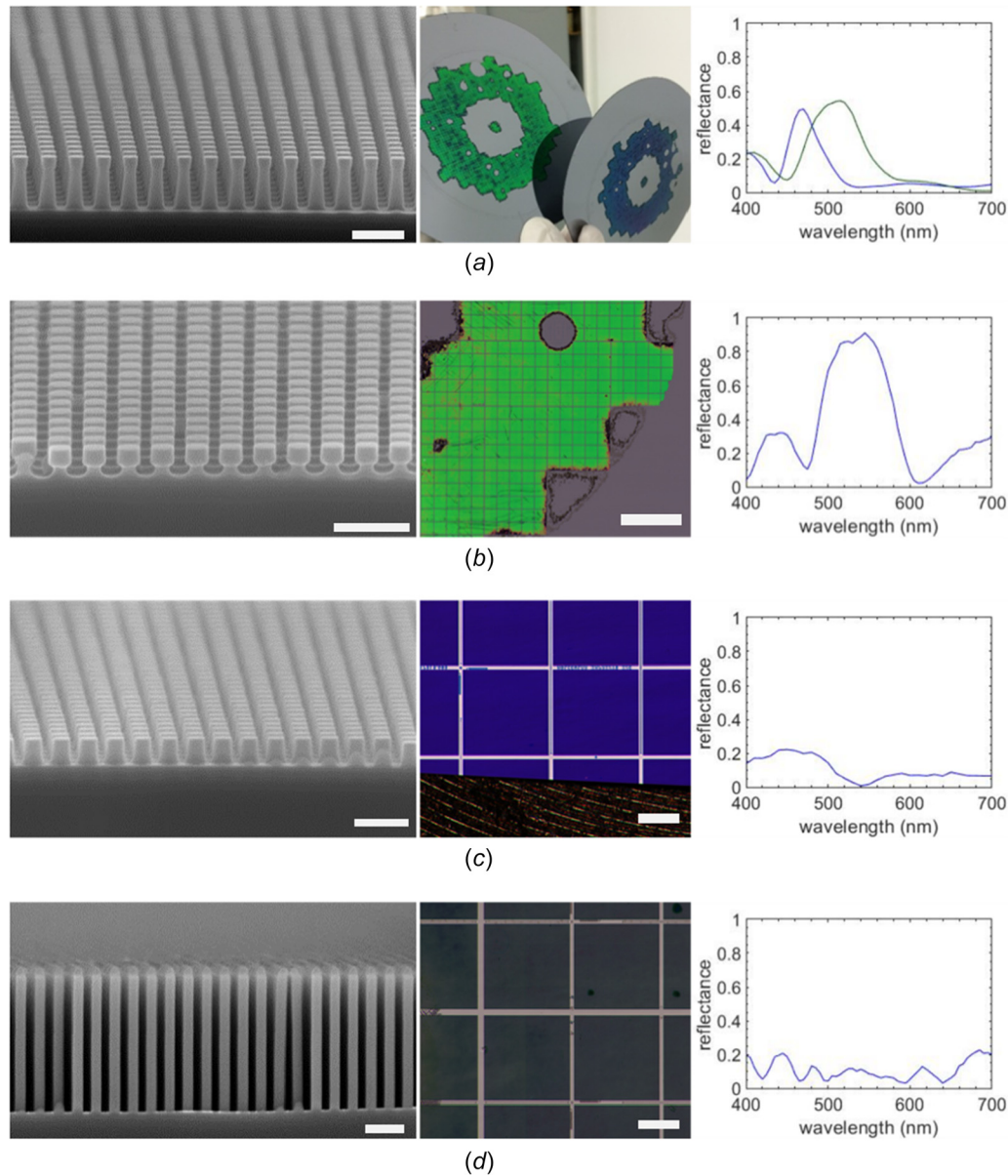


Fig. 1 Various Si nanopillar arrays, their visual appearances, and their reflectance spectra. The first column contains a cross section SEM of the structure, the second column contains an RGB image of the arrays, and the third column contains the reflectance spectrum of the array. Each row contains information about a different nanopillar array structure where the structures are as follows: (a) hourglass-shaped resonators (scale bar = 400 nm, wafer diameter = 100 mm). (b) Wineglass-shaped resonators (scale bars = 400 nm, 5 mm). (c) Truncated cones (scale bars = 400 nm, 500 μ m). (d) High aspect ratio nanowires made with MACE (scale bars = 400 nm, 500 μ m). There are two spectra for the hourglass-shaped pillars in (a), one for the blue wafer and one for the green wafer. The RGB image of the MACE nanowire array sample in (d) does not correspond to the spectra or the nanowires from the SEM image but is generally representative of the more ambiguous colors that the nanowire arrays create.

defects, and spectral signatures has not been focused on in the literature. Furthermore, computer vision methods can be used to classify defects and determine their root-cause based on the unique ways in which specific types of defects manifest, enabling process fault diagnosis and yield management. We will show how spectral imaging methods, specifically RGB imaging, can be coupled with computer vision algorithms to detect and classify defects in arrays of wine glass-shaped Si resonators which exhibit Mie resonance. This approach is marked by much higher throughput compared to traditional geometric metrology approaches, and therefore offers high value as a metrology approach in LNA manufacturing.

Methods

Experimental Setup. The wafer scale hyperspectral imaging system for reflectance measurements used here is shown in Fig. 2(a). The system uses a Tunable Light Source from Newport, Irvine, CA (model# TLS-300X) which directs light from a Xenon Arc Lamp through a monochromator, producing a beam of light which is tunable to different spectral bands in the visible spectrum and beyond. The beam is collimated by an achromatic doublet lens and then split by a beamsplitter. One half of the collimated beam is directed downward toward reflective samples which rest on a flat stage. The beam is reflected from the sample, passes again through the beamsplitter, and enters a telecentric lens attached to a 5-megapixel monochromatic CMOS camera from FLIR (#CM3-U3-50S5M). Lens telecentricity assures uniform angular collection over the entire field of view and constrains the measurement primarily to the specular reflection component. The system uses either a 0.367X lens (Edmund Optics #88-602) or a 3X lens (Edmund Optics #63-738) which produce FOVs of 19×23 mm and 2.4×2.8 mm, respectively, and pixel sizes of $9.4 \mu\text{m}$ and $1.2 \mu\text{m}$, respectively.

Typically, images are taken across the 400–700 nm wavelength range in steps of 5 nm (each having spectral bandwidth of 8 nm) producing 61 different images. The raw image intensities of the sample are calibrated using corresponding images of a reference bare Si wafer, producing reflectance images whose values are

scaled from 0 to 1 at each spectral band. Alternatively, the dataset can be thought of as being an image in which there is a reflectance spectrum located at every pixel. A conceptual illustration of the hyperspectral reflectance image is shown in Fig. 2(b).

While certain applications require the full acquired spectra [23], oftentimes it is convenient to convert the hyperspectral data to an RGB image. RGB images are much more compact, which significantly reduces compute cost. Furthermore, RGB imaging systems have much higher throughput considering that RGB cameras can acquire an entire image in a single shot, so it is advantageous to use RGB imaging in cases like the ones discussed in the Results section. Figure 2(c) shows an RGB image of a sample containing wine glass-shaped resonator arrays. RGB images like this one are created through a two-step conversion: (1) transformation from spectral reflectance values to tristimulus values via the “CIE 1931 2-deg XYZ” color matching functions [24] and (2) transformation from tristimulus values to RGB values via a transformation matrix [25].

Fabrication Process. As an illustrative example, we have fabricated wine glass-shaped Si nanopillar resonators. The fabrication scheme begins with the nano-imprint-based lithographic sequence shown schematically in Fig. 3. The first step in the lithographic sequence is nano-imprint patterning performed using Jet and Flash Imprint Lithography [1] in which the features are defined in an imprint resist mask. Once the imprint process has been completed, a “descum” reactive ion etch process (O_2 and Ar) is performed to remove the thin layer of resist, called the residual layer thickness (RLT), that remains between the features, exposing the underlying SiO_2 hardmask. After the descum etch, the pattern is transferred to the SiO_2 hardmask using an reactive ion etch process (CF_4 , Ar, and CHF_3). The template used in this work imprints square arrays of pillars that have a nominal feature diameter of 130 nm and 200 nm pitch. The pillar arrays are arranged into 1×1 mm squares which are distributed around the template in a donut shape with a central region of 5×5 squares. The groups of 1×1 mm squares can be seen in images of the sample throughout the paper. In between the patterned squares are regions typically referred to as

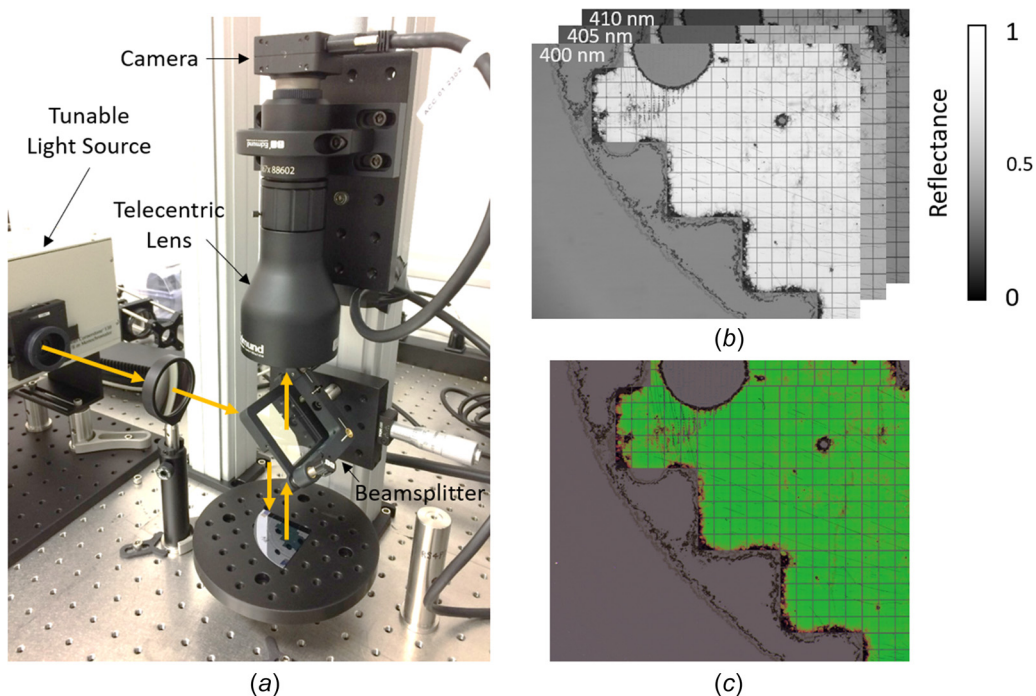


Fig. 2 (a) Hyperspectral imaging system, (b) representation of hyperspectral reflectance image dataset (field size is $\sim 19 \times 23$ mm), and (c) same dataset from (b) represented as an RGB image

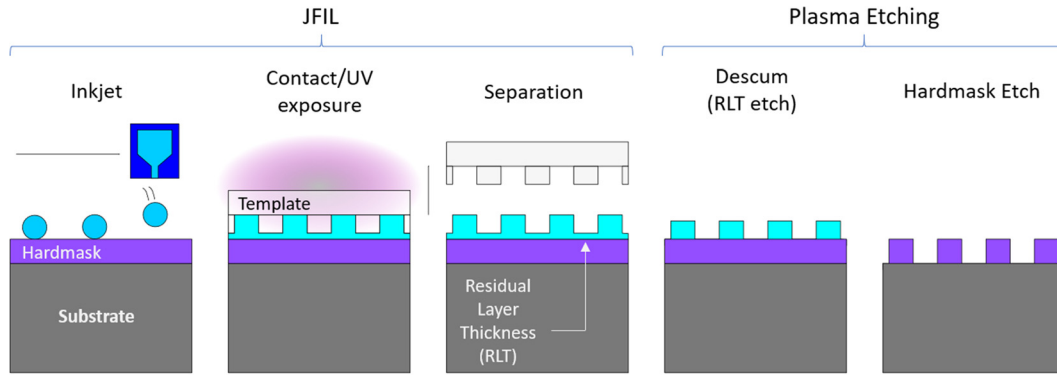


Fig. 3 General nano-impint process flow for Si nanopillar arrays

“streets” which contain bare Si and occasionally alignment markers.

Once the lithographic sequence is finished, the imprinted pattern is transferred into the Si substrate using plasma etching to create the wine glass-shaped structures. The wine glass fabrication sequence begins with an anisotropic Si etch (HBr and Cl_2). Then the sample is transferred to a deep Si etch tool and undergoes one cycle of the Bosch process [26] in which teflon sidewall protection is deposited, the horizontal regions are broken through with a physical etch (C_4F_8 , SF_6 , Ar), and then an isotropic etch (C_4F_8 , SF_6 , Ar) is conducted. The etch fabrication sequence and an exemplar cross section SEM image of the structures are shown in Fig. 4.

Results and Discussion

Types of Patterning Defects. The fabrication process for LNAs is relatively complex, and problems can arise in any of the individual steps. Defects can be random (e.g., due to the result of contamination), the result of nonoptimized recipes, the result of equipment malfunction, etc. Many of these defects uniquely manifest in the completed nanostructure arrays as visually identifiable features, and thus their root cause can often be diagnosed using computer vision schemes which classify defects based on various properties like color, size, shape, etc. We will demonstrate how effective our spectral imaging system has been for defect detection and classification, but first we discuss a few examples of different defect modes (etch delay/nonstart, imprint particle contamination, and imprint nonfilling). We discuss where these defects originate and how they uniquely manifest in completed devices as optical changes. With this background in mind, we will then describe computer vision schemes developed to detect and classify these defects in a sample of wine glass-shaped Si resonator arrays.

Etch Delay and Etch Nonstart. A delay in the start of the etch—referred to as “delayed etch start” or “etch delay”—can

occur if the area between the features in the etch mask has not been broken through prior to the etch that transfers the features into the substrate. This can occur, for instance, if the descum etch does not break through the RLT in some areas. This causes the start of the subsequent etch process to be delayed, because the underlying material is not initially exposed to the etchant. In the worst case, the etch will never begin because of the blockage—an “etch nonstart”—but since etch selectivity is never infinitely high, oftentimes the left-over mask material eventually etches away and then the substrate etch will begin—an etch delay. This causes features to receive less etch time than targeted, resulting in short features. In multistep etch processes, like the wine glass-shaped features, etch delay manifestation can be more complicated since the delay affects more than one subsequent etch.

When a uniform drop pattern is used in conjunction with a hole-tone template (used to imprint a pillar array pattern), etch delay commonly occurs at the edges of patterned areas. The mechanism behind this is shown in Fig. 5(a). Naturally, fluid volume builds up in the unpatterned region beyond the pattern edge and some of this build up gets squeezed into the nearby patterned area, increasing the RLT in this region. The increase happens in a graded fashion, resulting in a range of RLT thickness near the edge. An example of how this manifests in the wine glass-shaped arrays is shown in Fig. 5(b). The RLT increase in this case was severe enough to cause etch nonstart at the extreme edge of the pattern leaving behind a region of bare Si. Just within this region is a dark strip tracing the perimeter of the pattern, caused by etch delay. This region contains areas of partial breakthrough, like what is shown in Fig. 5(c), but mostly complete arrays of stubby, under-etched features, like what is shown in Fig. 6(c), which act as a graded index layer, increasing absorbance and creating the dark color. Inside this region is a thinner reddish strip caused by a lesser etch delay. The reddish color is likely the result of the resonators having slightly larger head diameter than those in the green areas—the result of feature thinning during the descum in areas where the RLT was thinner. The pattern eventually returns to the

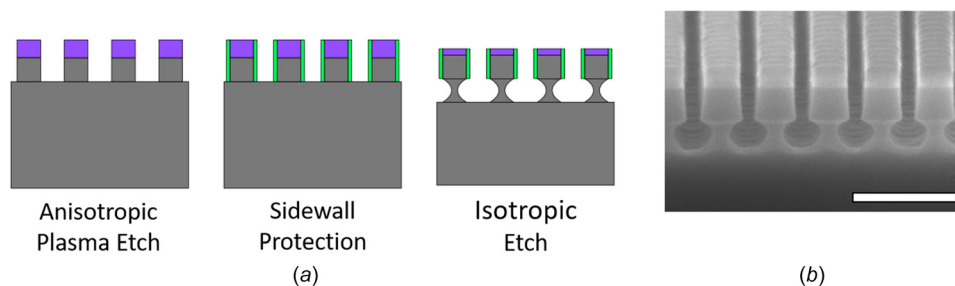


Fig. 4 (a) Schematic of etch fabrication sequence for Si wine glass nanopillars and (b) cross section SEM image of Si wine glass nanopillars (scale bar = 400 nm)

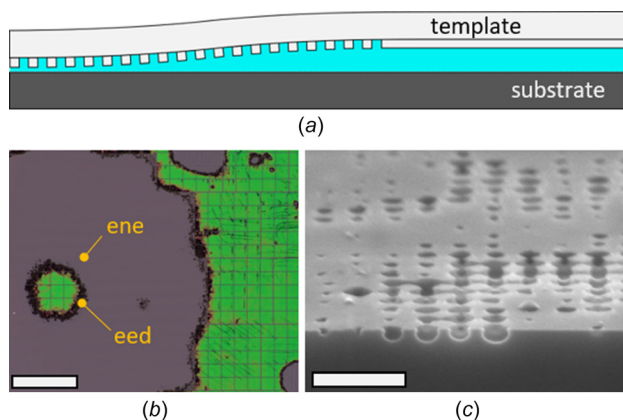


Fig. 5 (a) Schematic showing the mechanism behind etch delay and etch nonstart, particularly the edge forms of these defects. (b) RGB image of a sample containing wine glass-shaped resonator arrays in which there is a significant amount of edge etch delay (dark colored) such as at the point labeled “eed” and edge etch nonstart (gray colored) such as the missing square labeled “ene” (scale bar = 5 mm). Note that the template does not pattern the entire wafer. The central region of the wafer (center-left in the image), is supposed to be a 5×5 array of squares. The outermost squares here are left unpatterned due to etch nonstart. (c) Tilted cross section SEM image showing a region where the pattern has only just begun to break through—the effect of an extreme etch delay (scale bar = 600 nm). The image is actually taken from an instance of etch delay in a particle void perimeter.

nominal green color corresponding to the fully formed resonator arrays. It should be noted that Jet and Flash Imprint Lithography allows for nonuniform drop pattern distribution which can be used to largely mitigate etch delay [1].

Imprint Particle Contamination. The nano-imprint process results shown here are from an automated commercial tool, the Imprio 1100. This tool processes wafers in a clean chamber rated at better than Class 1, and the tool itself is placed in a Class 100 cleanroom. Despite being in a clean environment, extra care still must be taken to avoid particle contamination on the wafer or the template during imprint. For example, any manual handling of the wafers or templates prior to their introduction into the Imprio 1100 can lead to particles during the imprint process. Particle contamination between the template and the wafer can prevent the pattern from forming in the area surrounding the particle, as schematically illustrated in Fig. 6(a). The result is a large, unpatterned void on the wafer which exposes the underlying substrate, in this case Si. An example of a particle void on a wafer containing the wine glass-shaped Si resonator arrays is shown in Fig. 6(b). Because the template is fairly rigid, the resulting exclusion zone caused by a particle can have diameter of the order of one thousand times that of the particle itself [27], so the particle that caused this specific void was probably of the order of $3 \mu\text{m}$ in size. As seen in Fig. 6(b), particle voids are often surrounded by a dark perimeter region of etch delay, where the pattern is mostly occupied by arrays of stubby, under-etched features such as the ones shown in Fig. 6(c).

Imprint Nonfilling. Another common defect mode is the creation of small voids caused by nonfilling during the imprint process. Occasionally, bubbles of gas can get trapped inside the monomer fluid used to form the imprinted features or fluid can simply fail to spread to certain areas of the template, leaving a region of the wafer unpatterned as schematically illustrated in Fig. 7(a). These bubbles sometimes disappear if the spread time in the imprint process is increased, but many times the bubbles are stable over time, which may be due to a hydrophobic surface

contamination on the wafer that causes a dewetted region. Imprint nonfill voids are generally much smaller than particle voids, typically ranging from 10s to 100s of micrometer. They generally exhibit very sharp edges which are the result of the liquid “pinning” behavior during imprint—the fluid either fills a feature on the template or does not, so the edge of the defect is often a stepwise transition between patterned and unpatterned area which happens over a single period of the pattern itself. Nonfill perimeters can be graded, however, due to a patch-wise filling of individual features producing a perimeter region surrounding the void with a color in between that of the substrate and the normal patterned array. Pattern edges can be particularly vulnerable to non-filling if template-driven fluid spreading does not continue to the edge of the pattern, resulting in a specific type of defect called “edge nonfill.” The wafer discussed in Figs. 8 and 9 has a few instances of edge nonfilling.

Defect Detection/Classification in Si Resonator Arrays. To demonstrate the detection and classification of defects using spectral imaging, we have developed computer vision schemes for detecting and classifying defects in a wafer containing the Si wine glass-shaped resonator arrays. Figure 8(a) shows an RGB image of this 100 mm wafer which is stitched together from 19 sets of smaller field images taken of different portions of the wafer. Due to the Mie resonance effect in the pillar heads, the arrays create the vivid green color seen on most of the wafer. Based on the color, most of the wafer appears to contain the arrays, but there are many areas on the wafer that are clearly defective due to their departure from the nominal green color. These defective areas can be detected in a relatively straightforward manner by quantifying the green color and screening the image for colors that do not meet the definition of this green color. To do this, the RGB image is first converted to the hue, saturation, value (HSV) color space and then thresholded based on the following HSV parameters: $115 > H > 60$, $S > 140$, $V > 140$. This condition, which was tuned manually, essentially screens for pixels that are of sufficiently saturated and bright green color. Any pixels in the image not meeting this condition are then considered to contain defective arrays. Note that by “pixel,” we are referring to individual pixels in the image, not the device squares. The result of the defect detection scheme is shown in Fig. 8(b). Note that the large unpatterned areas of the wafer and the streets in between the squares are masked out of the analysis. The detection scheme is very effective at detecting the defects that are apparent in the original RGB

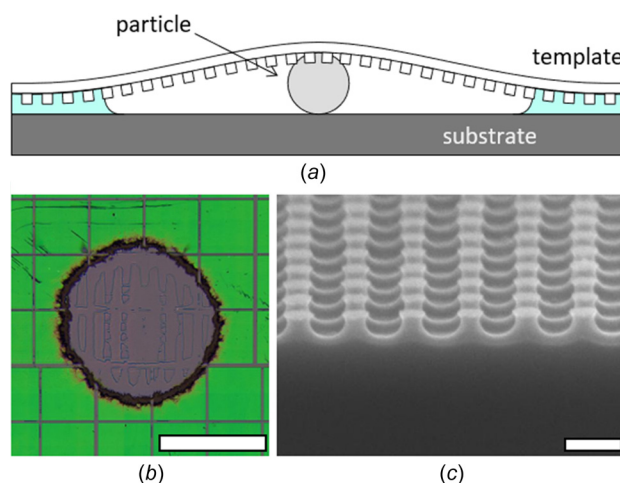


Fig. 6 (a) Schematic showing the effect of particle contamination on the nano-imprint process, (b) an RGB image of a sample containing Si wine glass-shaped resonator arrays with a void region caused by an imprint particle (scale bar = 2 mm), and (c) tilted cross section SEM image taken in part of the black ring region in (b) (scale bar = 200 nm)

image. We take the detection scheme one step further and demonstrate a mock device yield scenario for the wafer as shown in Fig. 8(c). Here, we simply treat each square as an individual device region and arbitrarily require that a device must have less than 10% of its pixels be defective for the device to yield.

After the defects are detected, they must be classified so that their root cause can be determined. Computer vision schemes for classification of the following defects in the wine glass array sample have been developed: imprint particle contamination, edge etch delay, edge etch nonstart, and edge nonfilling. The results of these classification schemes are shown Fig. 8(d). All schemes are preceded by an initial color indexing procedure which quantizes each pixel in the image to one of five colors (green, black, gray, red, or faded green). These colors are carefully chosen based on knowledge of the defect modes and how they manifest optically. Green, in this case, is the color assigned to the yielded pixels from the defect detection scheme. The rest of the colors are defined in Table 1. First, gray and black regions are found based on the thresholds described in Table 1. Gray, of course, is the color of bare Si which can be seen in particle voids, nonfilling voids, and etch nonstart. Areas affected by etch delay, like the pattern edges and the perimeters of particle voids, appear black. The remaining pixels are quantized to either red or faded green based on whichever color the pixels are closest to in terms of Euclidean distance in the HSV color space. The color red is associated with instances

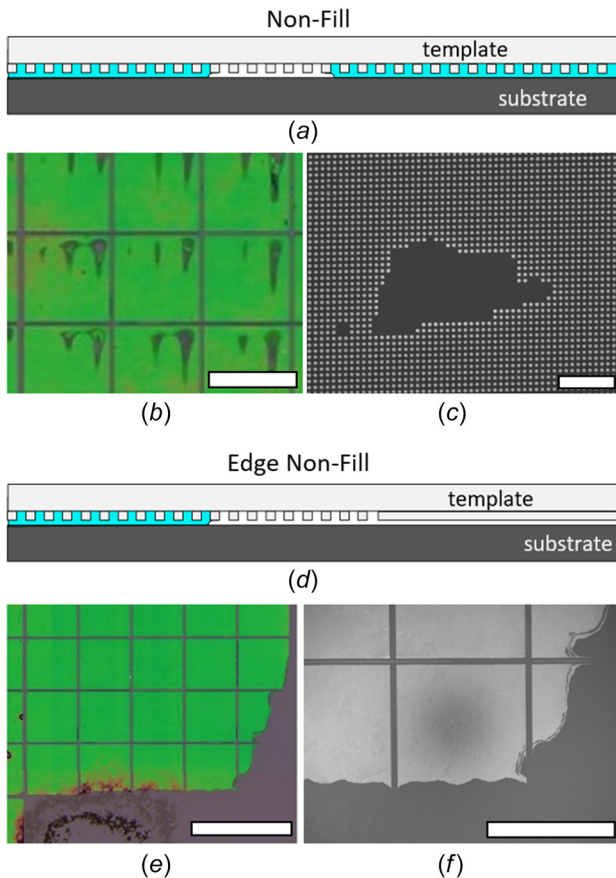


Fig. 7 (a) Schematic showing the mechanism behind nonfilling in the nano-imprint process, (b) an RGB image of a sample containing Si wine glass-shaped resonator arrays showing small void regions (gray-colored) caused by nonfilling (scale bar = 1 mm), (c) top-down SEM image of a nonfill void (scale bar = 2 μ m), (d) schematic showing the mechanism behind edge nonfilling in the nano-imprint process, (e) an RGB image containing an edge nonfill in a Si wine glass-shaped resonators sample (scale bar = 2 mm), and (f) top-down SEM image of the nonfill from (e) (scale bar = 1 mm)

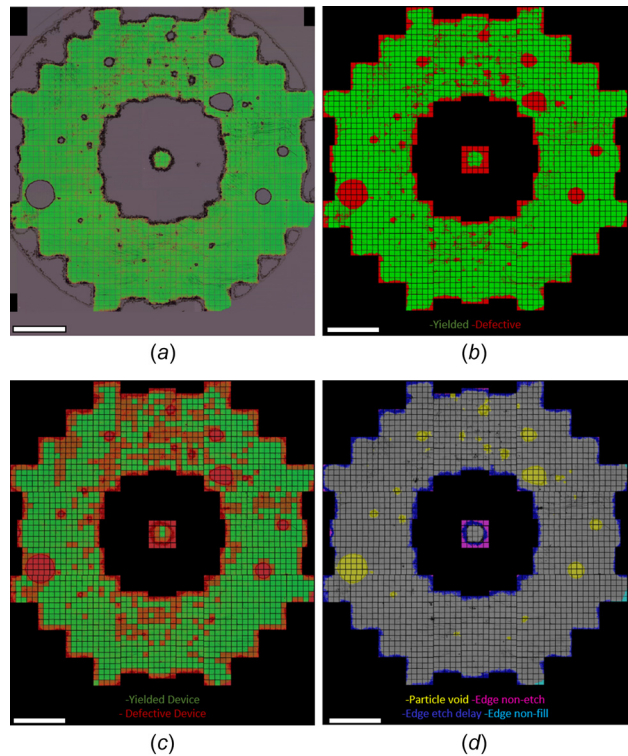


Fig. 8 (a) RGB Image of wafer containing wine glass-shaped Si resonator arrays. (b) Image showing defect detection results for the wafer in (a) with defects in red and yielded pixels in green. (c) Image showing device yield results with red being defective devices and green being yielded devices. (d) Image showing defect classification results with imprint particle defects in yellow, edge nonetch in magenta, edge etch delay in blue, and edge nonfill in turquoise. All scale bars = 1 cm.

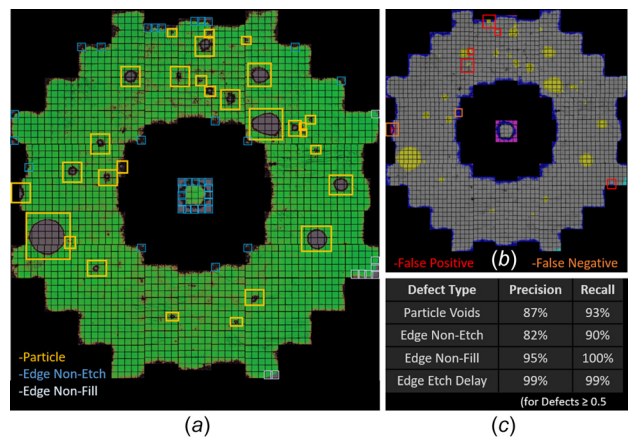


Fig. 9 (a) Close-up view of the RGB image of the wine glass arrays wafer (scale bar = 5 mm). (b) Labeled version of the image in (a) showing defect classification results with imprint particle defects in yellow, edge nonetch in magenta, edge etch delay in blue, and edge nonfill in turquoise (scale bar = 5 mm). (c) Close-up of a wrongly classified particle void defect (note the small circular outline in the center of the Si region which is the outline of a region masked by the particle during etch) (scale bar = 1 mm). (d) Side-by-side comparison of areas of the wafer containing nonfill defects with significant overlap from scratches (left) and no overlap from scratches (right) (scale bars = 1 mm).

of very mild etch delay, typically bordering black regions, but also found in many isolated instances as well. The faded green color is typically associated with areas having some fraction of missing features, such as at the edges of certain nonfilling voids. After color indexing, contiguous regions of pixels having one color or another are segmented, and then various properties of each region are determined, such as color, location, etc. Based on these region properties, the defects can be classified.

Classification of Imprint Particle Voids. The scheme for classifying imprint particle defects primarily makes use of the presence of the black ring of etch delay surrounding the gray particle exclusion zones. First, however, the scheme goes square by square through the color-indexed image, excluding edge square regions, and looks for squares that are occupied by greater than 90% gray pixels, and these regions are labeled as particle voids. This is done based on the observation that particle voids are the only cause of nonedge squares being completely voided out in this wafer. The scheme then finds the remaining gray regions, the gray regions are dilated so that their perimeter overlaps with the surrounding regions, and then the fraction of the region's perimeter which has each of the five different indexed colors is determined. If the fraction of black pixels surrounding the region is the highest, the region is assumed to be an imprint particle void.

The fact that the pattern is divided into squares makes the analysis significantly more complicated, because it breaks apart regions affected by the same particle defect. For instance, in certain squares only the ring region of the particle is present, and these are missed by the algorithm. So, a second algorithm is run on the squares that are in the immediate neighborhood of—or in other words, being directly adjacent to—the squares containing previously classified particle defects. First, the pixels that were previously classified are determined to be on the edge of the square or not. For the pixels that are on the edges of the squares, continuity is checked to see if a pixel with the color red, black, or gray exists directly across the street in each respective neighboring square. For instance, if the adjacent square is to the north, pixels from this north square sharing the same horizontal coordinates to those previously classified in the square to the south, would be screened for continuity. Where the continuity condition is met, these pixels are classified as particle defects. Subsequently, all the red, black, or gray pixels connected to the newly classified particle defect pixels are also classified as particle defects. The adjacency algorithm is run twice to not only capture continuity running north, south, east, and west, but also northeast, southeast, etc.

Classification of Edge-Related Defects. We have also developed a scheme for classifying different types of edge-related defects such as edge etch delay, edge etch nonstart, and edge nonfilling. This scheme looks at all the edge squares in the print area and determines whether there is a defective region with the color gray, black, or red overlapping with the edge of the square corresponding to the respective edge of the print area (e.g., the west edges of the west-most squares). If there is a gray region meeting this condition, the region is dilated (as was done in the particle scheme) and the colors of its perimeter pixels are analyzed. If the perimeter contains mostly black pixels, it is deemed an edge etch nonstart because this means its perimeter is shared with an

occurrence of etch delay. If its perimeter is mostly green pixels it is classified as an edge nonfill, because this means its perimeter is shared with normally patterned pillars, which is characteristic of nonfilling. Then, of the remaining regions, if the region is black or red it is deemed an edge etch delay. Finally, the classified defects are propagated to the adjacent neighboring squares based on continuity across the streets as was done before with the imprint particles.

Performance Quantification. In order to assess the performance of the classification algorithms, a manual count of each defect type on the wafer is taken and then the classification results from the algorithm are observed to count the number of true positives, false positives, and false negatives. In addition to the large, easily observable defects there are likely hundreds of small defects, so to make this analysis practical, only defects of size 0.5 mm or greater are considered. This procedure is documented in Fig. 10, which shows images of the wafer and our algorithm's classification results with manually placed annotations showing the defect locations in Fig. 10(a) and the locations of observed false positives and false negatives for all defect types in Fig. 10(b). Figure 10(c) then shows the results for calculations of precision and recall for each type of defect. Precision is defined as $tp/(tp+fp)$ and recall is defined as $tp/(tp+fn)$ where tp is number of true positives, fp is number of false positives, and fn is number of false negatives. The classification algorithm consistently has slightly better recall than precision, because the false positive rate is slightly higher than the false negative rate. This means that for a given defect type, the algorithms tend to over-classify, but generally do a good job of not missing defects. Edge etch delay defects (also 0.5 mm or greater) are left unannotated in Fig. 10 because nearly every edge device has this defect. The classification results for edge etch delay are observed to have one false positive and two false negatives resulting in ~99% precision and recall.

Discussion of Failure Modes. Closer views of the imaging and classification results are shown in Figs. 9(a) and 9(b). The

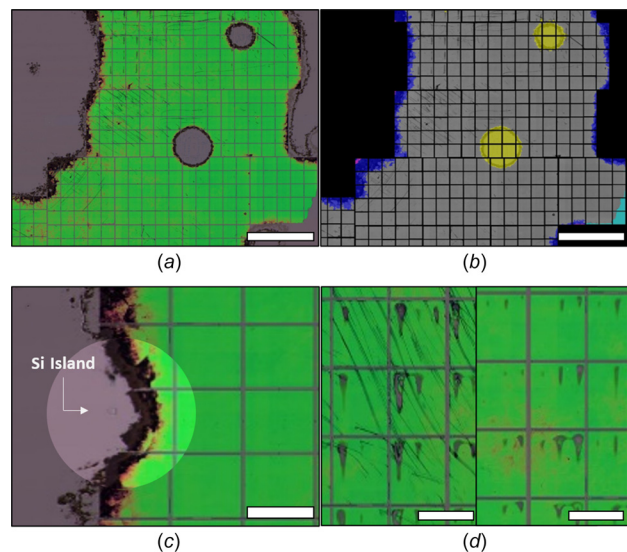


Table 1 HSV threshold values and color centroids for indexing of colors

	H	S	V
Black	—	—	$V < 75$
Gray	—	$S < 50$	$V > 75$
Red	120	119	55
Faded green	50	90	50

Note: For black and gray, color thresholds are defined, whereas for red and faded green, the color centroids are defined.

perimeter analysis approach works quite well for classification of the edge defects and particle voids, but with some shortcomings. In particular, the method for differentiating between edge etch nonstart/delay and particle voids was primarily based on whether or not the defect had occurred in the edge squares. This approach works well in this wafer but is vulnerable to failure in future wafers which could have particles on edges and/or etch nonstart in the central region of the pattern. In fact, there is a particle void on the west edge of this wafer that was incorrectly classified as a etch nonstart/delay defect. Figure 9(c) shows this defect. Visually, we were able to identify this error based on the presence of an outline of a small, circular gray region within the defect. This is a region in which, due to the presence of the particle, drop spreading was prevented, and thus was exposed directly to the subsequent Si etch. The region is surrounded by an area that was masked by drops which did spread and thus were masked during the etch. Though difficult to see, regions like these are present in many of the small/medium sized voids on the wafer. The void region of larger particle defects also contains regions masked by partially spread drops, like what can be seen in Figs. 6(b) and 10(a). These void features, which are not observed in etch nonstart voids, are especially visible when the oxide hardmask is still intact because of thin film interference exhibited by the oxide films capping the top of the masked regions. Although the images in this analysis were taken postoxide hardmask removal, spectral imaging could be conducted prior to oxide hardmask removal to take advantage of this feature for differentiating between particle voids and etch nonstart regions.

The particle void scheme can also mistakenly select for some nonfill defects (typically smaller than 0.5 μm) which curiously have a significant percentage of dark pixels on their perimeter. This is unexpected behavior for nonfilling voids as, unlike with particle voids, etch delay is not expected to occur at their perimeter. Indeed, most of the nonfill voids on the wafer appear to be surrounded by green or faded green. However, there are a number of nonfill voids with a high fraction of black in their perimeter, although generally they exist in areas where there is a large number of scratches present, overlapping with the nonfills. This suggests that the scratches may be the main cause of the unexpected black pixels—possibly via feature collapse. A side-by-side comparison of nonfills overlapping with scratches and isolated nonfills is shown in Fig. 9(d). To suppress this inaccurate classification, small voids were filtered out of the analysis with an image open operation [28]. However, this has the consequence of missing small particle voids with diameter $< 100 \mu\text{m}$. The presence of overlapping defects generally presents a difficult challenge, because although defects follow a set of rules quite closely when isolated, the rules are violated in unexpected ways when defects overlap.

Further Discussion. As described in the preceding sections, the computer vision approaches developed for defect detection and classification are specific to particular defect types and their optical manifestations. For deployment to the manufacturing line, it is likely that the effectiveness of the classification algorithms can be optimized as well as generalized by applying machine learning techniques. Since the methods developed here roughly follow a decision tree structure, decision tree learning methods (e.g., random forests) would be a natural extension of this classification approach. Features would still need to be chosen carefully and based on the effectiveness of the perimeter feature, this feature would likely be utilized in a machine learning model but may be modified and accompanied by additional features. Alternatively, it may be possible to use deep learning methods (e.g., convolutional neural networks), particularly since the images are always taken under the same conditions, although there may be a challenge with obtaining sufficiently large datasets for model training.

The examples shown have been conducted “at line,” in which defect detection/classification was performed after the structures were made. Using an in situ imaging system, however, defects

could be identified in real time. A spectral imaging system capable of video rate frame capture—an RGB video camera, for instance—could be used to characterize samples during etching. Etch delay, for instance, could then be identified in regions that are observed to change color late in the etch process. Furthermore, a correlation between nanopillar geometry and color, whether empirical or model-based, could provide feedback on instantaneous etch rate and uniformity, offering grounds for real-time process control schemes.

Conclusions

The results presented in this article demonstrate the use of spectral imaging and computer vision methods for defect detection, classification, and root-cause analysis of Si nanopillar arrays. The large field of view of spectral imaging methods coupled with their micrometer-scale imaging resolution and sensitivity to nm-scale feature geometric variations allows for high-throughput characterization, which means defect detection/classification can be done quickly enough to cover a significantly higher percentage of total device area compared to traditional scatterometry techniques, SEM, and AFM which generally have low throughput. Specific defect modes including imprint particle contamination, etch delay, and imprint nonfilling, were discussed in terms of their origin as well as how they manifest in completed devices as optical changes with unique color, spatial orientation, etc. Based on these features, rule-based computer vision schemes were developed to detect and classify these various defects in a wafer containing wine glass-shaped Si resonator arrays created using nano-imprint and plasma etching. The rule-based schemes were quite effective, but machine learning methods could be used in the future to offer a more sophisticated and generalizable approach. Although the results were demonstrated for Si nanopillar arrays, similar nanophotonic effects exist for many other types of LNAs, and thus this technique can be applicable to a wider range of structures such as wire-grid polarizers and metal mesh grids.

Acknowledgment

This work was performed at the Texas Nanofabrication Facility (TNF) at The University of Texas at Austin (UT) which includes the Microelectronics Research Center and the NASCENT nanodevice-manufacturing fab (nm-Fab). TNF is a member of the National Nanotechnology Coordinated Infrastructure (NNCI), which is supported by the National Science Foundation. The NASCENT Center is a nanosystems engineering research center also funded by the National Science Foundation. The authors would also like to thank the T.W. Whaley, Jr. Friends of Alec Endowed Scholarship for partly funding Brian Gawlik during this work.

Funding Data

- National Science Foundation (NSF) (Grant Nos. EEC-1160494 and ECCS-1542159; Funder ID: 10.13039/100000001).
- Scalable Nanomanufacturing Program (NSF) (Grant No. ECCS-1120823; Funder ID: 10.13039/100000001).

References

- [1] Sreenivasan, S. V., 2017, “Nanoimprint Lithography Steppers for Volume Fabrication of Leading-Edge Semiconductor Integrated Circuits,” *Microsyst. Nanoeng.*, **3**(1), p. 17075.
- [2] Ahn, S. H., Yang, S., Miller, M., Ganapathisubramanian, M., Menezes, M., Choi, J., Xu, F., Resnick, D. J., and Sreenivasan, S. V., 2013, “High-Performance Wire-Grid Polarizers Using Jet and Flash™ Imprint Lithography,” *J. MicroNanolithography MEMS MOEMS*, **12**(3), p. 031104.
- [3] Pallares, R. M., Su, X., Lim, S. H., and Thanh, N. T. K., 2016, “Fine-Tuning of Gold Nanorod Dimensions and Plasmonic Properties Using the Hofmeister Effects,” *J. Mater. Chem. C*, **4**(1), pp. 53–61.

- [4] Catrysse, P. B., and Fan, S., 2010, "Nanopatterned Metallic Films for Use as Transparent Conductive Electrodes in Optoelectronic Devices," *Nano Lett.*, **10**(8), pp. 2944–2949.
- [5] van de Groep, J., Spinelli, P., and Polman, A., 2012, "Transparent Conducting Silver Nanowire Networks," *Nano Lett.*, **12**(6), pp. 3138–3144.
- [6] Cao, A., Sudhölter, E., and de Smet, L., 2013, "Silicon Nanowire-Based Devices for Gas-Phase Sensing," *Sensors*, **14**(1), pp. 245–271.
- [7] Field, C. R., In, H. J., Begue, N. J., and Pehrsson, P. E., 2011, "Vapor Detection Performance of Vertically Aligned, Ordered Arrays of Silicon Nanowires With a Porous Electrode," *Anal. Chem.*, **83**(12), pp. 4724–4728.
- [8] Zhao, H., "Vertical Silicon Nanowire Arrays for Gas Sensing," Massachusetts Institute of Technology, Cambridge, MA, p. 97.
- [9] Park, H., and Crozier, K. B., 2015, "Vertically Stacked Photodetector Devices Containing Silicon Nanowires With Engineered Absorption Spectra," *ACS Photonics*, **2**(4), pp. 544–549.
- [10] Park, H., Dan, Y., Seo, K., Yu, Y. J., Duane, P. K., Wober, M., and Crozier, K. B., 2014, "Filter-Free Image Sensor Pixels Comprising Silicon Nanowires With Selective Color Absorption," *Nano Lett.*, **14**(4), pp. 1804–1809.
- [11] Park, H., and Crozier, K. B., 2013, "Multispectral Imaging With Vertical Silicon Nanowires," *Sci. Rep.*, **3**, p. 2460.
- [12] Kim, W.-K., Lee, S., Hee Lee, D., Hee Park, I., Seong Bae, J., Woo Lee, T., Kim, J.-Y., Hun Park, J., Chan Cho, Y., Ryong Cho, C., and Jeong, S.-Y., 2015, "Cu Mesh for Flexible Transparent Conductive Electrodes," *Sci. Rep.*, **5**(1), p. 10715.
- [13] Chang, S., Oh, J., Boles, S. T., and Thompson, C. V., 2010, "Fabrication of Silicon Nanopillar-Based Nanocapacitor Arrays," *Appl. Phys. Lett.*, **96**(15), p. 153108.
- [14] Cherala, A., Chopra, M., Yin, B. A., Mallavarapu, A., Singhal, S., Abed, O., Bonnacaze, R. T., and Sreenivasan, S. V., 2016, "Nanoshape Imprint Lithography for Fabrication of Nanowire Ultracapacitors," *IEEE Trans. Nanotechnol.*, **15**(3), pp. 448–456.
- [15] Na, H., and Endoh, T., 2013, "A Multi-Pillar Vertical Metal–Oxide–Semiconductor Field-Effect Transistor Type Dynamic Random Access Memory Core Circuit for Sub-1 V Core Voltage Operation Without Overdrive Technique," *Jpn. J. Appl. Phys.*, **52**(4S), p. 04CE08.
- [16] Chung, H., Kim, H., Kim, H., Kim, K., Kim, S., Song, K.-W., Kim, J., Oh, Y. C., Hwang, Y., Hong, H., Jin, G.-Y., and Chung, C., 2011, "Novel 4F² DRAM Cell With Vertical Pillar Transistor(VPT)," Proceedings of the European Solid State Device Research Conference (ESSDERC), IEEE, Helsinki, Finland, pp. 211–214.
- [17] Sun, Y., Yu, H. Y., Singh, N., Le, T. T., Gnani, E., Baccarani, G., Leong, K. C., Lo, G. Q., and Kwong, D. L., 2011, "Junction-Less Stackable SONOS Memory Realized on Vertical-Si-Nanowire for 3-D Application," Proceedings of International Symposium on VLSI Technology, Systems and Applications, Hsinchu, Taiwan, Apr. 25–27, pp. 1–2.
- [18] Proust, J., Bedu, F., Gallas, B., Ozerov, I., and Bonod, N., 2016, "All-Dielectric Colored Metasurfaces With Silicon Mie Resonators," *ACS Nano*, **10**(8), pp. 7761–7767.
- [19] Gawlik, B. M., Cossio, G., Kwon, H., Jurado, Z., Palacios, B., Singhal, S., Alù, A., Yu, E. T., and Sreenivasan, S. V., 2018, "Structural Coloration With Hourglass-Shaped Vertical Silicon Nanopillar Arrays," *Opt. Exp.*, **26**(23), p. 30952.
- [20] Zeiss, "ZEISS MultiSEM 505/506 the World's Fastest Scanning Electron Microscopes," Zeiss, Oberkochen, Germany, accessed Feb. 1, 2020, <https://www.zeiss.com/microscopy/us/products/scanning-electron-microscopes/multisem.html>
- [21] Flauraud, V., Reyes, M., Paniagua-Domínguez, R., Kuznetsov, A. I., and Bruger, J., 2017, "Silicon Nanostructures for Bright Field Full Color Prints," *ACS Photonics*, **4**(8), pp. 1913–1919.
- [22] Seo, K., Wober, M., Steinvurzel, P., Schonbrun, E., Dan, Y., Ellenbogen, T., and Crozier, K. B., 2011, "Multicolored Vertical Silicon Nanowires," *Nano Lett.*, **11**(4), pp. 1851–1856.
- [23] Gawlik, B. M., Barrera, C., Yu, E. T., and Sreenivasan, S. V., 2020, "Hyperspectral Imaging for High Throughput, Spatially Resolved Spectroscopic Scatterometry of Silicon Nanopillar Arrays," *Opt. Express*, **28**, pp. 14209–14221.
- [24] Institute of Ophthalmology, 2019, "Colour Matching Functions," Institute of Ophthalmology, London, UK, accessed Nov. 3, <http://cvrl.ioo.ucl.ac.uk/cmfs.htm>
- [25] Ford, A., and Roberts, A., 1998, "Colour Space Conversions," p. 31.
- [26] PlasmaTherm, 2019, "Deep Silicon Etching," PlasmaTherm, accessed Feb. 17, 2021, <http://www.plasma-therm.com/etch-dse.html>
- [27] Singhal, S., Grigas, M. A., and Sreenivasan, S. V., 2016, "Mechanics-Based Approach for Detection and Measurement of Particle Contamination in Proximity Nanofabrication Processes," *ASME J. Micro Nano-Manuf.*, **4**(3), p. 031004.
- [28] Mathworks, "Imopen," Mathworks, Natick, MA, accessed Feb. 1, 2020, <https://www.mathworks.com/help/images/ref/imopen.html>